Directional and seasonal variations of seismic ambient noise in southeastern Canada and the NE USA

Omid Bagherpur Mojaver [ID] and Fiona Darbyshire [ID]

Centre de recherche GEOTOP, Université du Québec à Montréal, CP 8888 succursale Centre-Ville, Montréal, QC H3C 3P8, Canada.
E-mail: omid.bagherpur@gmail.com

SUMMARY

Ambient seismic noise is mainly generated in oceans through the interactions between the atmosphere, ocean waves and the solid Earth. Study areas located near the edges of continents are thus subject to receiving an inhomogeneous noise field that could cause bias in ambient noise wave attenuation measurements and tomography studies. Ambient seismic noise characteristics across SE Canada and the NE USA are studied in detail at a regional scale for the first time, due to the availability of over 2 yr of data (2013–2015) recorded at 69 broad-band seismographs. This large, dense data set allowed us to use a back-projection technique to investigate both the azimuthal and temporal variations of the ambient noise. This method is based on a statistical analysis of signal-to-noise ratios (SNRs) of the waveforms in the calculated empirical Green's functions for pairs of stations. We propose a new method of analysing the SNR by modifying the already existing concept of fan diagrams to include both causal and acausal components of the noise cross-correlograms in the analysis. We investigate directional and seasonal variations of the recorded noise data across the study area at the three main passbands of the seismic noise spectrum including the secondary microseisms (SM; 3–10 s), the primary microseisms (PM; 10–30 s), and the seismic hum (Hum; 30–300 s). We observe that the strongest and weakest signals are received at the SM and Hum bands, respectively. Considering the results of this study along with those from previous studies, we conclude that the strongest seismic noise arrivals at the three passbands investigated in this study (i.e. SM, PM and Hum) are generated at different locations in the Atlantic, Pacific and Arctic oceans.

Key words: North America; Time-series analysis; Seismic interferometry; Seismic noise; Surface waves and free oscillations.

1 INTRODUCTION

Passive seismic tomography techniques are extensively used in studies of Earth's structure. Data for these methods are provided by either earthquakes or ambient seismic noise. As earthquake sources are not ideally distributed in space and time, ambient seismic noise provides a different important source to study the Earth's seismic structure at different scales, with a wide depth coverage that includes the crust (e.g. Macquet *et al.* 2014; Kuponiyi *et al.* 2017), uppermost mantle lithosphere and asthenosphere (e.g. Yang & Ritzwoller 2008; Kao *et al.* 2013; Haned *et al.* 2016), and into the lower-mantle and core–mantle boundary (e.g. Boué *et al.* 2013; Poli *et al.* 2015; Retailleau *et al.* 2020). In the case of core–mantle boundary phases, the role of ambient noise has, however, been disputed; Tkalčić *et al.* (2020); Wang & Tkalčić (2020a, b) suggest instead that earthquake coda is the main source of energy in the cross-correlated signals. Foundation of ambient seismic noise tomography (ANT) was laid down after discovering that Green's functions can be extracted from

ambient seismic noise cross-correlation functions (e.g. Shapiro & Campillo 2004). Reliability of these empirical Green's functions (EGFs) is dependent on the validity of the homogeneous noise distribution assumption. In reality, however, ambient seismic noise is not a homogeneous field as the strongest noise generation sources are located in the oceans (Gutenberg 1936). Using long-duration data sets and modern data processing techniques serves to minimize the non-uniform noise distribution effect, but it may still cause bias in the measurements of seismic velocity and crustal attenuation resulting from the analysis of noise cross-correlation functions (e.g. Bensen *et al.* 2007; Yang *et al.* 2008; Tsai 2011; Chen *et al.* 2016). Some studies suggest that even a non-uniform noise distribution can allow for unbiased estimates of traveltimes (e.g. Chen *et al.* 2016). In particular, in study regions where the crustal seismic structure is more complex and variable, it is suggested that the bias due to an inhomogeneous ambient noise distribution is minimized (Sadeghisorkhani *et al.* 2017). In ambient noise tomography studies, careful attention to ray path coverage (particularly the

azimuthal distribution of interstation paths), will also considerably reduce such bias (Bagherpur Mojaver & Darbyshire 2022). Nevertheless, persistent localized sources located off the great-circle path of the station pair could generate signals arriving earlier than the interstation surface waves, causing the arrival times and amplitudes of the emerging surface waves to be different in the positive and negative cross-correlation lags (e.g. Guo *et al.* 2020). Resulting interstation phase-velocity measurements using asymmetric EGFs thus could be biased, especially in regions with smaller velocity variations and at wavelengths comparable to the interstation distance (Sadeghisorkhani *et al.* 2017). Understanding noise source distribution and adopting a proper processing scheme are especially crucial in modern full-waveform inversion applied to noise correlation functions, and crustal wave attenuation estimation (Cupillard & Capdeville 2010; Harmon *et al.* 2010; Fichtner 2014; Stehly & Boué 2017). Therefore, it is important to study the noise field characteristics and the potential effects of different pre-processing techniques on the noise cross-correlation functions. To this end, we use a back-projection technique, based on statistical analysis of the energy of emerging signals (Tian & Ritzwoller 2015; Wang *et al.* 2021). We note that, using a back-projection method and a single seismic array, it is not possible to infer the exact locations of dominant noise sources. However, this approach enables us to investigate the emerging signal strength, the azimuthal content, and their variations over time. The main motivation of this study was to conduct an ambient noise directionality and seasonality analysis across SE Canada and the NE USA, similar to that carried out on the west coast of North America by Tian & Ritzwoller (2015). Our seismograph network is comparable in spatial extent and density, but we are able to extend the investigation further by using multi-year data sets for the first time.

1.1 Previous studies

Directional and seasonal variations of ocean-generated ambient seismic noise are typically studied in terms of their frequency content (e.g. Tian & Ritzwoller 2015; Chen *et al.* 2016). The strongest and weakest seismic noise signals are observed at 3–30 s (microseisms) and 30–300 s (seismic hum) periods respectively (Köhler *et al.* 2011; Carvalho *et al.* 2019; Nakata *et al.* 2019). The main passbands investigated in studies of ambient noise source characterization are the secondary microseisms (SM, 3–10 s), the primary microseisms (PM, 10–30 s) and the seismic hum (Hum, 30–300 s). The SM and PM are also called double-frequency and single-frequency microseisms, respectively. This is because the PM has a spectral peak near to that observed for ocean swells, whereas the SM has a dominant peak frequency approximately double that of the spectral peak of the ocean waves (Cessaro 1994).

With the exception of a few studies that suggest a deep ocean origin for the PM (e.g. Köhler *et al.* 2011), it is generally accepted that the PM are mainly generated from the direct interaction between ocean waves and sloping sea floor near coasts (e.g. Hasselmann 1963; Cessaro 1994; Tian & Ritzwoller 2015; Chen *et al.* 2016). Gualtieri *et al.* (2019) found that identifying PM source locations using stations closest to coasts can be misleading as the longer period PM signals could be dominated by arrivals from distant coasts, located thousands of kilometers away from the stations. On the other hand, the SM are interpreted as generated by nonlinear interaction of two ocean waves of similar periods meeting from opposite (or near-opposite) directions, creating a pressure column that transfers the wave energy to the seafloor (e.g. Longuet-Higgins

1950; Hasselmann 1963; Tian & Ritzwoller 2015; Chen *et al.* 2016; Carvalho *et al.* 2019). This process can occur in both shallow water and deep ocean areas, so the location of SM generation is still under debate. Some studies suggest deep sea (pelagic) generation (e.g. Tian & Ritzwoller 2015; Guo *et al.* 2020), while some other studies support shallow water generation for the SM (e.g. Köhler *et al.* 2011; Gerstoft & Tanimoto 2007). Some authors also identified both pelagic and near-coastal generation for the SM band (e.g. Cessaro 1994; Ardhuin *et al.* 2011; Chen *et al.* 2016). The Hum is the least understood part of the ambient noise spectrum. It is believed to be caused by the direct interaction between the ocean waves and sloping seafloor, and mainly generated along the shelf breaks (Ardhuin *et al.* 2015), coastlines or bathymetric highs (Ermert *et al.* 2021).

1.2 Methodologies

Different techniques have been used to locate ambient seismic noise sources at different passbands. The grid search method, also known as the migration method, is based on minimizing the travel time misfit between stations and candidate noise sources, and has been successfully used to obtain noise source locations in the Atlantic and Pacific oceans (e.g. Shapiro *et al.* 2006; Zeng & Ni 2010). Using a three-component plane wave beamforming technique, Behr *et al.* (2013) inferred noise sources for Rayleigh and Love waves in New Zealand and suggested both deep water and near coastal source regions for the secondary microseism band. We use a 'back-projection' method to study the directional and seasonal variations of the arriving ambient seismic noise to the study area, based on statistical analysis of the energy of emerging signals (e.g. Tian & Ritzwoller 2015; Wang *et al.* 2021). While the exact location of the dominant noise sources cannot be inferred from this analysis, one advantage of the back-projection technique is that the analysis is relatively easier and faster to conduct compared to the grid search and the beamforming methods. This is because in this method, only signal-to-noise ratio (SNR) values for the emerging signals in the EGFs need to be calculated, and it does not require advanced mathematical and statistical computations. As a result, one can perform directionality and seasonality analysis for various EGF data sets resulting from different pre-processing techniques and (relatively) quickly compare the results before using those EGFs as inputs to a tomography study.

2 STUDY AREA

Our study area includes a region covering southeastern Canada and the northeastern USA (Fig. 1). This area was tectonized since ~1 Ga with the latest tectonic activity associated with the proposed passage of the Great Meteor Hotspot at ~110 Ma (e.g. Sleep 1990). On average, about 450 earthquakes occur in eastern Canada each year and less than 0.1 per cent of these events have $M_w > 4$ (source: https://www.earthquakescanada.nrcan.gc.ca/zones/eastcan-en.php). During the two year period of this study, 168 events with $2.5 < M_w < 4.5$ have been listed in the earthquake record database beneath our station coverage area, only two of which having $M_w > 4$ (source: https://www.earthquakescanada.nrcan.gc.ca/index-en.php). The occurrence of these small intraplate local earthquakes is especially frequent along the St. Lawrence rift system, throughout New Brunswick, and beneath the offshore Grand Banks. In addition to small local/regional earthquakes, large teleseismic events and possible unwanted local transients should
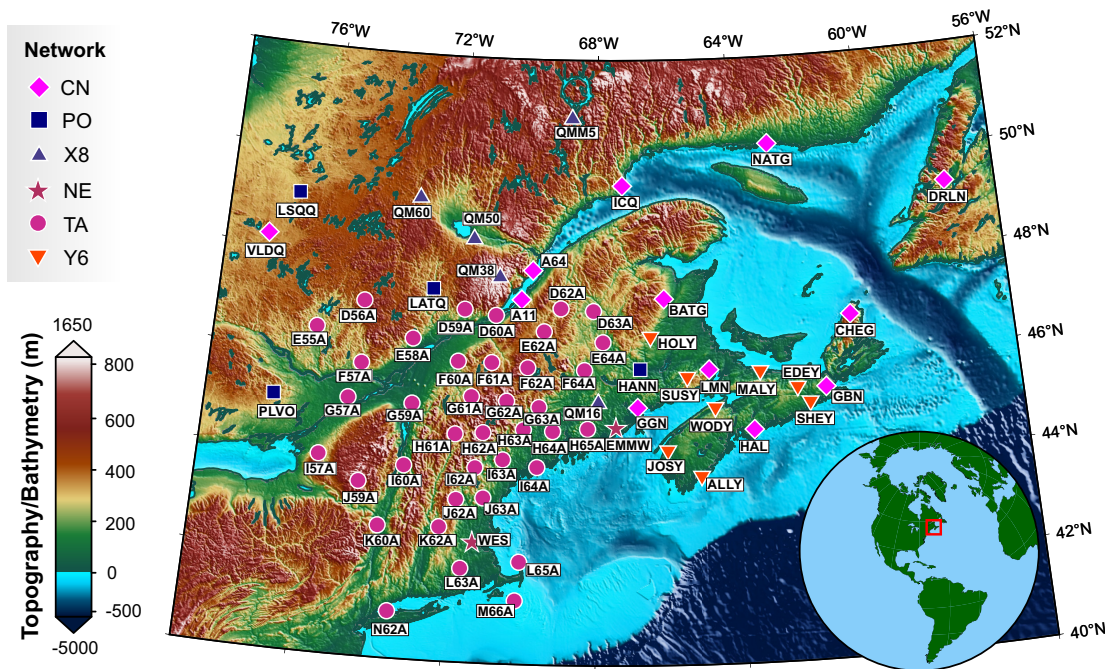
Figure 1. Map of study area and 69 stations belonging to six different seismograph networks used in this study.

be removed from the ambient noise records before conducting the analysis of directionality and seasonality (Section 3).

Being located in the northern hemisphere West Atlantic Extratropical Cyclone region, our study area experiences severe weather events such as strong coastal waves and storms (Poan *et al.* 2018). These events can in turn provide local sources of ambient seismic noise generation. Therefore, a careful investigation of ambient seismic noise seasonality and directionality is extremely valuable for investigation of the proposed source regions, and noise generation mechanisms at different frequency bands of the seismic noise spectrum.

3 DATA SETS AND DATA PROCESSING

The ambient seismic noise data set used in this study is from 2013 August 1 to 2015 November 1 (823 d) provided by the vertical channels of 69 broad-band seismic stations belonging to six seismograph networks (Fig. 1). The seismic networks are the Canadian National Seismograph Network (CN, 12 stations; Geological Survey of Canada 1989), New England Seismic Network (NE, 2 stations; ASL/USGS 1994), USArray Transportable Array (TA, 38 stations; IRIS Transportable Array 2003), Portable Observatories for Lithospheric Analysis and Research Investigating Seismicity (PO: POLARIS, 4 stations; Eaton *et al.* 2005) and QM-III experiment (X8 and Y8 networks, 13 stations; Menke *et al.* 2012; SEIS-UK 2013). An extensive investigation of seismic ambient noise in our study area is limited by the fact that the majority of the data sets (i.e. ∼75 per cent) are provided by the stations belonging to the TA and QM-III networks that were only operational between the years 2013 and 2015. That said, this 2-yr period of continous ambient noise records is adequate to enable us to perform a detailed analysis of ambient seismic noise directionality and seasonality.

The time-series for each station are publicly available and were acquired as daily records. We followed a conventional data processing scheme for single-station processing of the ambient noise data prior to computing the noise cross-correlation functions. This

procedure included instrument response removal, resampling of all time-series to a sample frequency of 1 Hz, one-bit normalization to remove earthquake signals and possible local transients (Shapiro & Campillo 2004; Shapiro *et al.* 2005; Yao *et al.* 2006), and spectral whitening to flatten the ambient seismic noise in the frequency domain (Bensen *et al.* 2007). We chose to apply one-bit normalization instead of other available techniques such as traditional methods of manually removing earthquakes, the running absolute mean method (e.g. Bensen *et al.* 2007), or setting a clipping threshold for the time-series amplitudes (e.g. Sabra *et al.* 2005). Although this pre-processing method may reduce sensitivity to detecting short-term and transient sources (Chen *et al.* 2016), it still is a generally accepted method that is used in numerous ambient seismic noise studies (e.g. Stehly *et al.* 2006; Yao *et al.* 2006; Kuponiyi *et al.* 2017).

In order to produce EGF data sets, we first cross-correlate the processed daily records to obtain noise cross-correlation functions (NCFs). We then stack those NCFs to generate the final EGFs. By stacking different sets of daily NCFs, we can acquire seasonal data sets that are useful to conduct the seasonality analysis.

4 AZIMUTHAL VARIATIONS OF SIGNAL TO NOISE RATIO

For a cross-correlation time-series between two stations A and B ($R_{A,B}$), the causal part of the resulting cross-correlogram (positive lags) indicates the outgoing signal from station A to B, whereas the acausal part (negative lags) is the incoming signal from station B to A. Assuming that the ambient seismic noise field is perfectly homogeneous, we should observe the same signal for both causal and acausal parts of the interstation NCFs. In reality, however, the negative and positive lags in the NCFs are different, indicating an inhomogeneous noise distribution (Fig. 2). Therefore, we can infer the azimuth of the more dominant noise source by comparing the acausal and causal signal energies for each EGF. Inferring the azimuths of the dominant noise sources by analysing a collection of
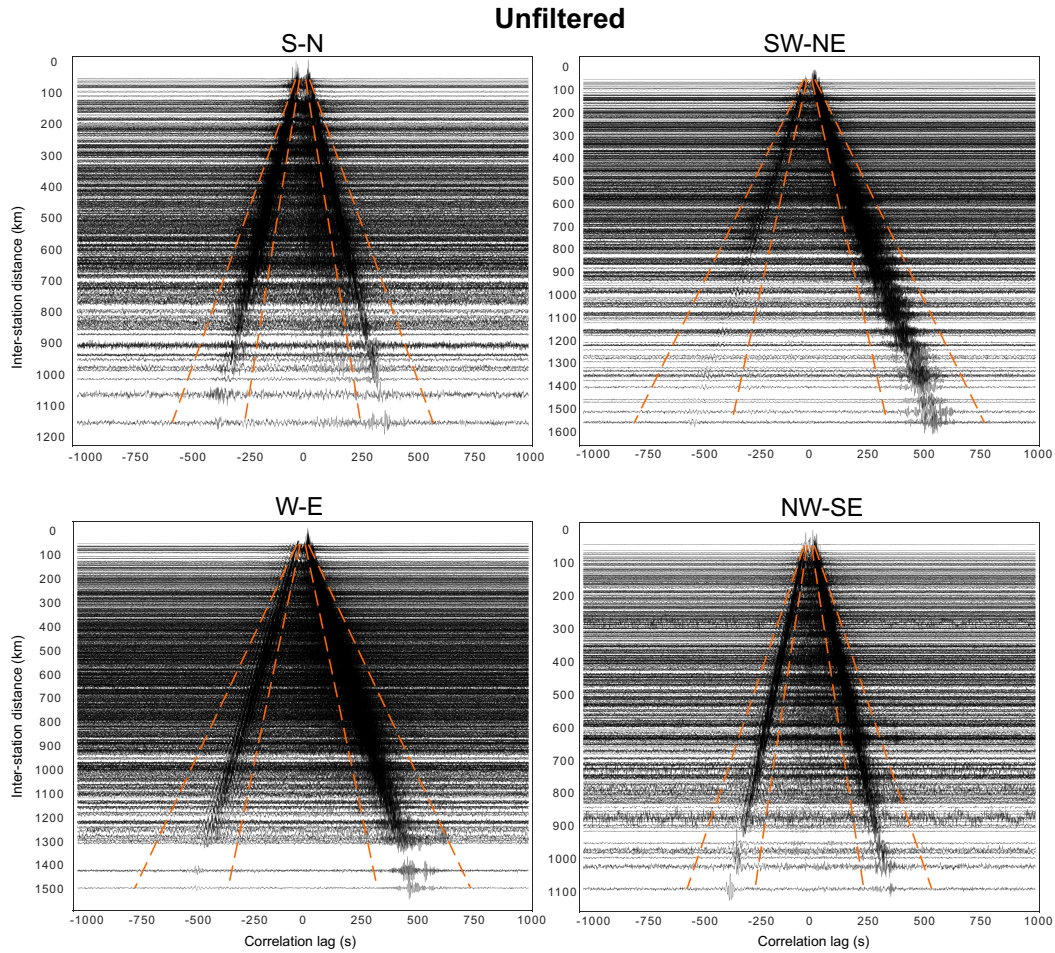
Unfiltered

Figure 2. Unfiltered EGFs grouped into four main interstation orientations (azimuthal bin size of 45°). The EGFs in this figure are presented such that the causal signals (positive lags) represent the energies traveling from N to S (S–N subplot), from NE to SW (SW–NE subplot), from E to W (W–E subplot) and from SE to NW (NW–SE subplot). The orange dashed lines indicate moveout velocities of 2 and 4.5 km s^{-1}. Similar figures for bandpass filtered EGFs are available in the Supporting Information (Figs S1 and S2).

EGFs is much more challenging due to the effects of site-dependent background noise level, different interstation distances, and variable numbers of individual daily NCFs contributing to the final inter-station EGFs (stack number; e.g., Chen *et al.* 2016). It is thus important to account for these effects when using back-projection techniques to locate dominant noise sources.

In order to reduce the effect of site-dependent background noise level, SNR is used as this parameter includes root mean square (RMS) of the background noise in its formulation. The SNR is expressed as

$$\text{SNR(dB)} = 20 \log \frac{\text{RMS}_{\text{signal}}}{\text{RMS}_{\text{noise}}},$$

where $\text{RMS}_{\text{signal}}$ and $\text{RMS}_{\text{noise}}$ are the RMS for signal and noise time-series windows, respectively. We compute SNR values for all EGFs separately for the causal and acausal signals. The signal and noise windows have the same window length for each EGF, but vary between different inter-station EGFs. The signal/noise window length for each EGF with a given station separation is calculated using 2 and 4.5 km s^{-1} moveout velocities. These values were chosen after making sure that they include the dispersive signal wavetrains at different passbands for the entire EGF data sets (Fig. 2; Supporting Information Figs S1 and S2). It is still possible to have coherent ambient noise signals outside the selected envelopes, mainly caused

by multipathing and scattering. In addition, surface wave coda may also contribute to the generated NCFs, though this effect should be minimized during pre-processing. Once the signal/noise window size for each EGF is calculated (Fig. 3), we place the centre of the window at the maximum amplitude of the signal within the range defined by the moveout velocities (Fig. 3). Although previous back-projection studies used peak amplitude as opposed to $\text{RMS}_{\text{signal}}$ to represent the propagating signal energy (e.g. Tian & Ritzwoller 2015), we argue that the surface wavetrains are dispersive and using $\text{RMS}_{\text{signal}}$ in the calculation of SNR is a valid representative parameter for the total energy of the signals. While this definition does not allow direct comparison of the SNR values in this study with the previous studies that use peak amplitude in their SNR formulation (SNR values using our definition are typically smaller in comparison), we will still be able to compare the final results for noise directionality. Using our definition, SNR values greater than 3 imply that a Rayleigh wave signal exists above the noise level.

Having calculated the SNR values for causal and acausal components of the entire EGF data sets, we correct the values for variable interstation distances and stack numbers, to make the SNR values comparable using the experimental normalizing formulations explained by Tian & Ritzwoller (2015) and Chen *et al.* (2016). Accordingly, we correct the SNR values by multiplying each value by the correction factor of $\sqrt{d/d_0} \times \sqrt{n_0/n}$, where d is the
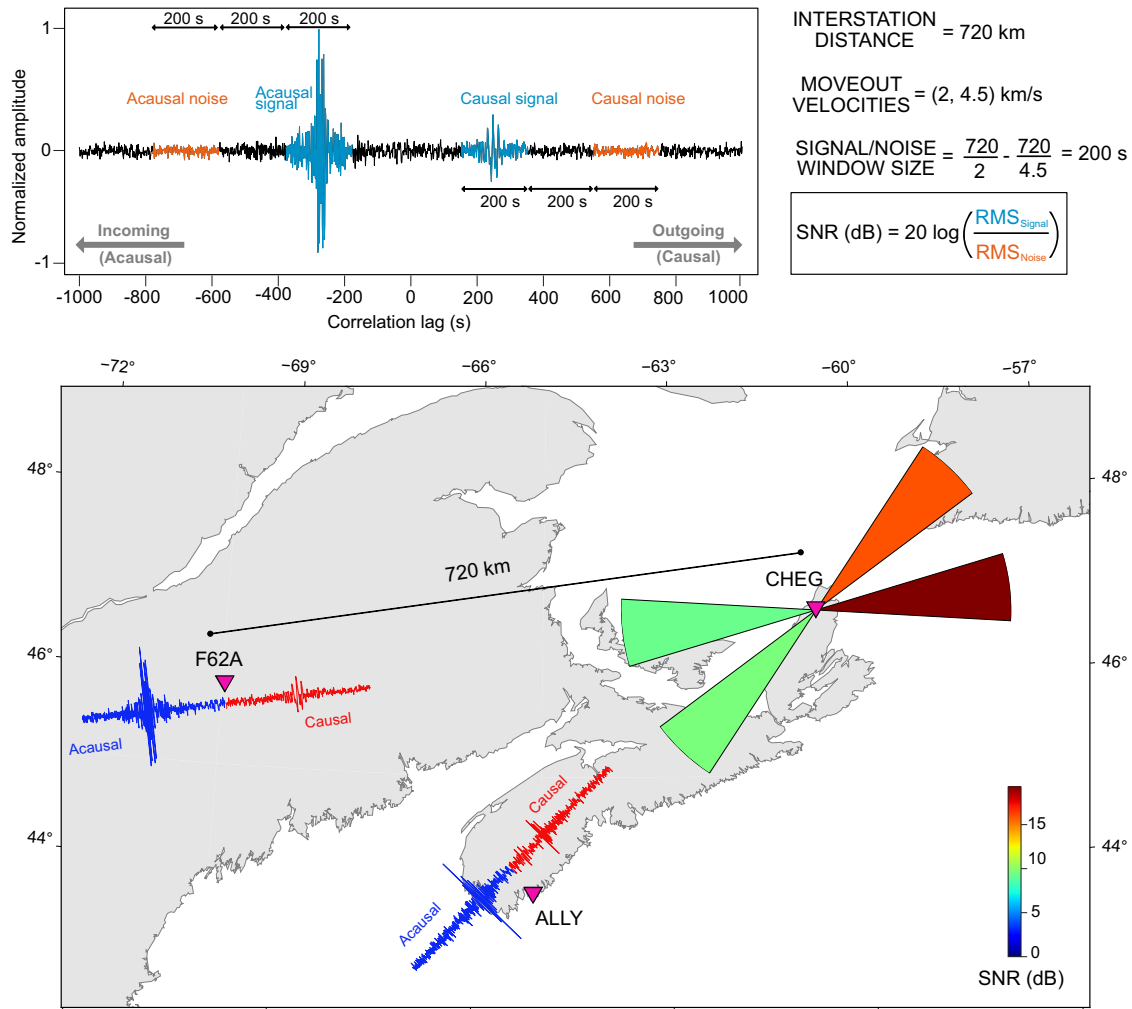
Figure 3. Example for SNR calculation and fan diagram representation. The panel at the top left represents the time-series of stacked noise cross-correlation function (EGF) for station pair F62A-CHEG. Signal/noise window size depends on the inter-station distance and the example calculation for this station pair is shown at the top right (see the text for more information). Bottom panel illustrates an example fan diagram definition resulting from two EGFs for station CHEG in Cape Breton Island, Nova Scotia.

inter-station distance, d_0 is the reference inter-station distance, n is the stack number and n_0 is the reference stack number. We set the reference values of d_0 and n_0 to their median values for the entire EGF data sets (Fig. 4). In this paper, hereafter, by 'SNR' we refer to the corrected values of this parameter.

The idea of fan diagram representation to analyse azimuthal and temporal variations of ambient seismic noise was first proposed by Tian & Ritzwoller (2015). Fan diagrams are polar bar charts with equal-length bars that are colour-coded to show the average SNR variations received at stations from different azimuthal bins. In the results presented in this study, we set the bar width (i.e. azimuthal bin size) in the final fan diagrams to 10°, hence 36 coloured bars build a complete-set fan diagram. If more than one SNR value is collected for each azimuthal bin, the average of the values is used for the final presentation. It is also possible to have missing bars if a station does not have full azimuthal coverage. This issue can usually be overcome by generating average fan diagrams related to a group of stations which then can be placed at an average coordinate location. In the process of producing data sets for generating fan diagrams (i.e. calculating SNR values for causal and acausal signals), EGFs resulting from stacking both $NCF_{A, B}$ and $NCF_{B, A}$ are used, where

A and B are the first and second stations and NCF is the noise cross-correlation function. For each EGF, causal and acausal SNR values are used as two fan diagram data points at the second station, and the results are illustrated by two opposing fan diagram bars oriented along the interstation path (Fig. 3). The fan diagram bar attributed to the causal SNR points to the first station, and the bar attributed to the acausal SNR points to the opposite direction. Following this, high SNR bars in the final fan diagrams would point to the direction of the dominant noise sources. Since both causal and acausal signals are used in the generation of fan diagrams, we can generate a rose-diagram for each fan diagram to show the original causal/acausal data distribution; in other words, explaining how many causal/acausal data points have contributed to the observed average SNR value of each azimuthal bin (Fig. 5). Our definition has two major differences with that presented by Tian & Ritzwoller (2015): (1) We use more data as we exploit both causal and acausal parts of the data sets whereas only causal parts are used in their method. (2) In their definition, high SNR bars point away from the dominant noise source locations whereas, in our definition, the high SNR bars point toward the noise sources. We believe that this new method serves better to show directional variations as both acausal
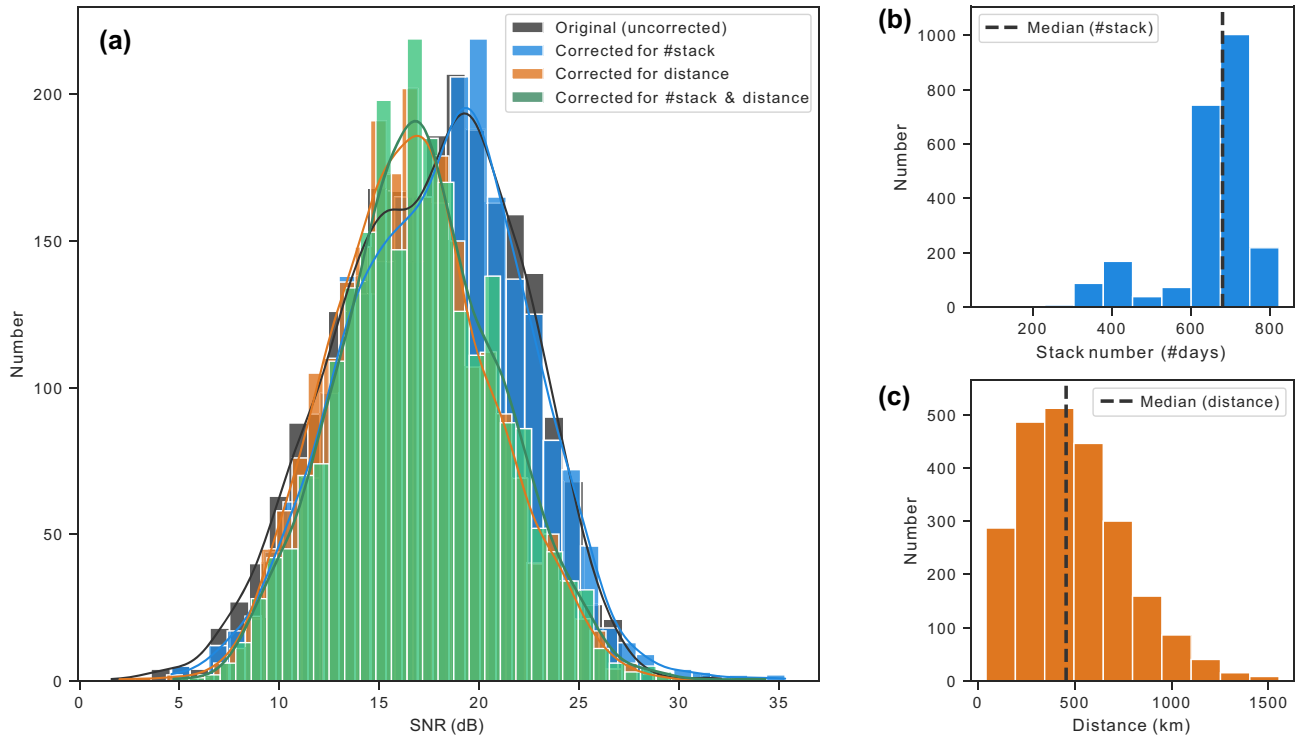
Figure 4. Calculated SNR values for the symmetric component of the EGFs before and after applying the corrections for variable interstation distance and stack number (see the text for more information). (a) SNR distributions; (b) stack number distribution; (c) interstation distance distribution.
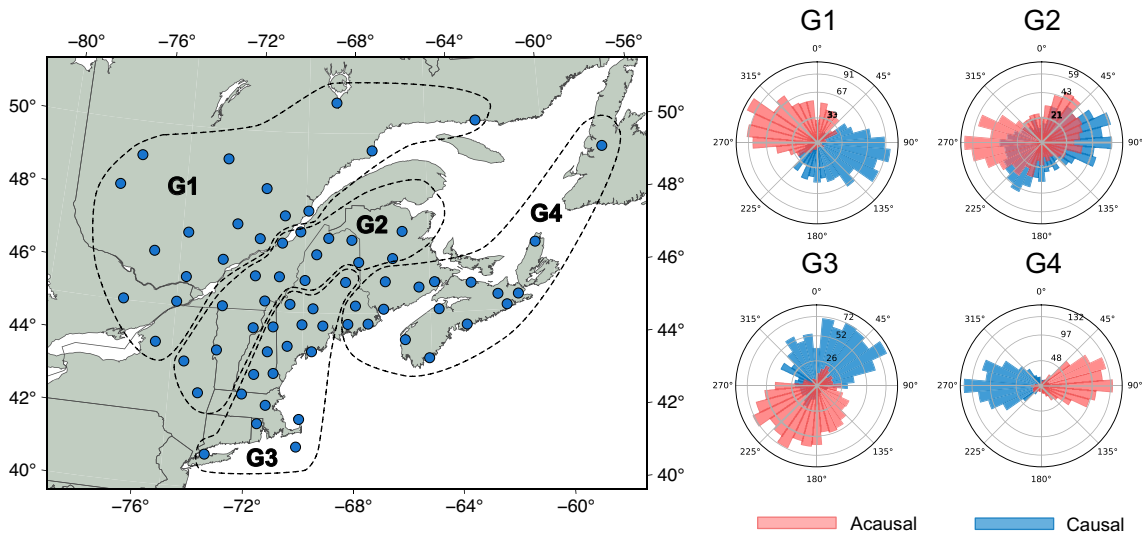

Figure 5. Average fan diagram station groups (left), and the corresponding rose diagrams (right) representing the data distribution of both causal and acausal components contributing to the generation of the average fan diagrams. Rose diagrams for individual stations are also available in the Supporting Information (Figs S13–S20).

and causal signals contribute to the value of average SNR in each bar of a fan diagram for each station. Comparing the fan diagram presentations, the difference becomes especially more evident at stations located near the edges of the seismic arrays.

In addition to the fan diagrams generated for individual stations, we also grouped the station fan diagrams into four groups, namely G1–G4, and calculated the corresponding average fan diagrams. Acausal/causal distribution of the data used in the generation of station and group fan diagrams are illustrated using rose diagrams (Fig. 5; Supporting Information Figs S3–S5). Although the selection

of stations for each group and the choice of designing four station groups rather than a different number was subjective, we made sure that all groups include as full an azimuthal coverage as possible with a similar number of contributing stations placed in each group (i.e. 17–18 stations). As shown in Fig. 6, two of these groups encompass stations near the Atlantic coast (groups G3-G4), and two farther away from the Atlantic coastal regions (groups G1 and G2). The majority of the stations in groups G1 and G2 are also located in an area with a different tectonic heritage than that of groups G3 and G4 (Peri-Laurentian versus Peri-Gondwanan domains;
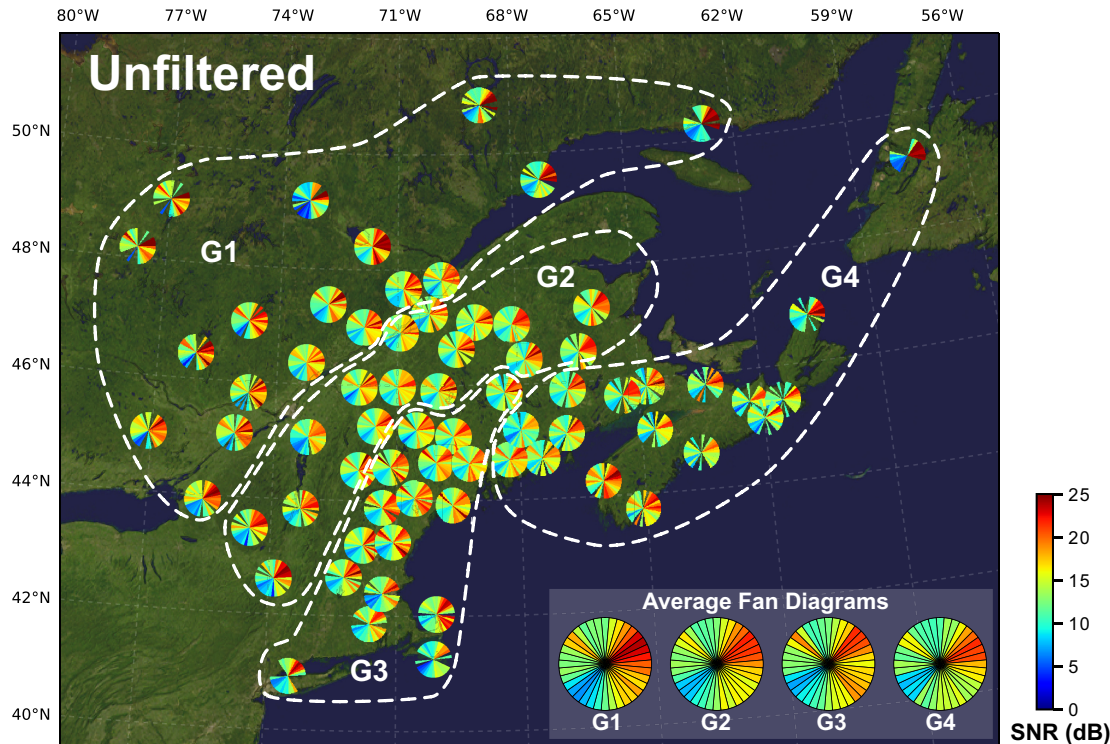
Figure 6. Fan diagrams for the unfiltered EGF data sets. Group averaged fan diagrams are illustrated at the bottom right. Maps of fan diagrams for the SM (3–10 s), PM(10–30 s), Hum (30–300 s) and their related subpassbands are available in the Supporting Information (Figs S6–S12).

e.g., van Staal & Barr 2012). Our analysis suggests that by grouping stations and measuring average fan diagrams, measurement errors will be considerably reduced (Supporting Information Figs S13–S20).

5 RESULTS

In this paper, we base our explanation of the results and the discussion mainly on the group average and total-data set average fan diagrams, and not on the fan diagrams generated for the individual stations. This is because in the generation of the average fan diagrams, a significantly larger number of EGFs are used (Fig. 5; Supporting Information Figs S3–S5), and thus they present the variations with considerably lower uncertainties (e.g. Supporting Information Figs S13–S20). In the following two subsections, we explain our observations in terms of variations in signal strength and azimuthal content for the full-stack EGF data sets (directionality analysis) as well as for the EGF data sets resulting from different temporal NCF stacking configurations (seasonality analysis).

5.1 Directionality analysis

The main directionality analysis results of this paper are presented using fan diagrams. An example map of fan diagrams for the unfiltered EGF data sets is presented in Fig. 6, whereas the maps of fan diagrams for the bandpass filtered data sets (SM, PM and the Hum) are available in the Supporting Information (Figs S6–S12). A comprehensive summary of the results with additional subpassbands investigated in this study is presented in Fig. 7. The input EGFs to produce the fan diagrams for the directionality analysis are generated from stacking available daily NCFs for all the station pair records in the two year period of this study.

The average fan diagrams at different passbands suggest that noise-generated Rayleigh wave signals arrive from all directions at all passbands (SNR > 3; Fig. 7). By comparing the bandpass filtered results (Supporting Information Figs S6–S12) to the unfiltered results (Fig. 6), we observe that the strongest and weakest signals of the ambient seismic noise spectrum are generated at the secondary microseism band and seismic hum band respectively (Fig. 7). The weakest noise signals in this study (3 < SNR < 4) are observed at the seismic hum band propagating from the east (azimuths between 70° and 90°), and the strongest signals with SNR > 25 dB arrive from the northeast at the SM band (∼60° azimuth).

At the SM band (3–10 s), the minimum signal strength with SNR of ∼7–8 dB is received from the southwest (centred at 230° azimuth). Investigating fan diagrams at this passband, we note at least two main dominant noise sources with very different characteristics (Fig. 7; Supporting Information Fig. S6). The strongest noise signals arrive from the northeast with the high SNR band in the fan diagrams covering a wide range of azimuths from the north to southeast with the peak centred at 60°. A much weaker, but still pronounced, narrow signal propagates from the northwest to our study area with a maximum SNR centred at 310°. We also investigated two subpassands for the SM: 3–5 s and 5–10 s. At the longer period subpassband, 5–10 s, the observed pattern of the noise strength distribution is very similar to that observed at 3–10 s, which is consistent with the 7 s maximum peak spectrum suggested for the SM by previous studies (e.g. Cupillard & Capdeville 2010). At the shorter period subpassband 3–5 s, however, the narrow northwest signal is absent.

The azimuthal content and signal level of the noise arriving from different directions at the PM band (10–30 s) is generally different from that observed at the SM band. The PM band has a similar minimum signal strength as that observed at the SM band (∼7–8 dB), but the maximum strength signals arriving at this passband
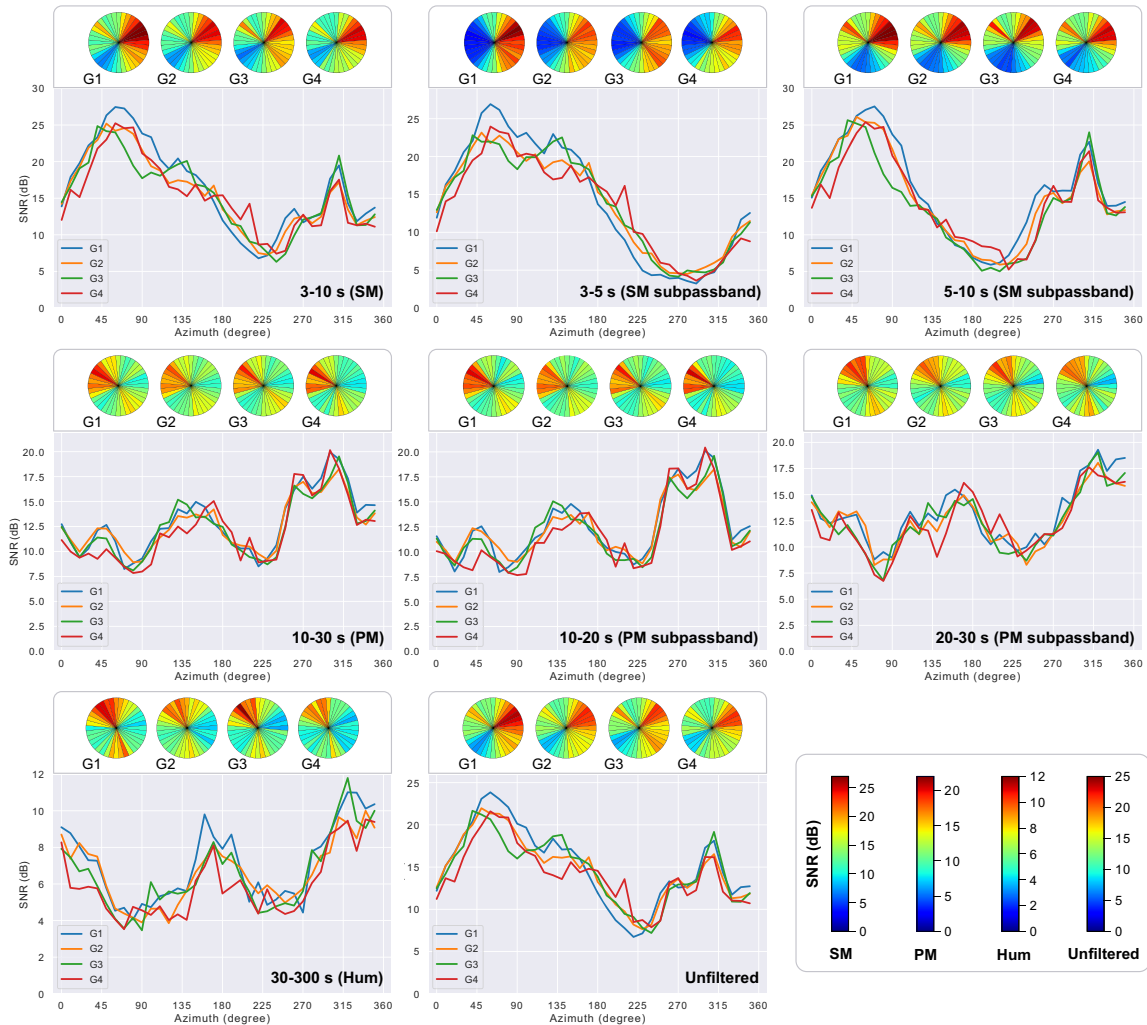
Figure 7. The directionality analysis results for the group averaged fan diagrams, G1–G4, at different passbands and subpassbands investigated in this study.

are relatively weaker than those observed at the SM band (∼20 dB; maximum SNR centred at ∼300° azimuth). We observe at least three dominant sources for the PM, two of the stronger ones arrive from the west with their azimuths centred at 270° and ∼300°, with the average SNR values of 17 and 20 dB respectively. A relatively weaker but still significant source at this passband arrives from the south to the southeast with a maximum SNR of 15 dB and centred at ∼150° azimuth. We also investigated two subpassbands of 10–20 and 20–30 s for the PM band. Having compared the patterns of fan diagrams for these two subpassbands with the original PM band, we observe that the fan diagrams for subpassband 10–20 s are very similar to that observed at the original 10–30 s PM band. The noise strength variations at subpassband 20–30 s, however, are relatively less correlated with the patterns observed for 10–30 and 10–20 s. They are more similar to the patterns observed for the Hum instead, but with considerably higher signal strength.

Although the weakest signals in the ambient seismic noise spectrum are associated with the Hum band (30–300 s), our results suggest that these signals exist and arrive from all directions (SNR > 3), at least for a set of EGFs based on a two year NCF stack. The azimuthal content of the dominant noise signals arriving at the study area at the Hum band has a similar character to that observed for the PM band; it is especially well-correlated with subpassband 20–30 s. The strongest Hum signals arrive from northwest to the

north azimuths with average SNR values of 10–11 dB centred at ∼320°. Another significant Hum source is also located in the south, characterized by a relatively narrower and weaker signal arriving from ∼170° azimuth.

5.2 Seasonality analysis

In order to analyse the temporal variations of the arriving ambient seismic noise signals in terms of their strength and azimuthal content, we generated a series of EGF data sets based on stacks of NCFs for different time periods. To describe monthly variations of the seismic noise, the NCFs for each month (January to December) for years 2013 to 2015 were stacked to generate monthly EGF data sets and the corresponding fan diagrams for each station. We produce the final monthly fan diagrams by averaging those from all the individual stations. Figs 8–10 illustrate the results of this analysis. In addition, we also stacked NCFs belonging to the four northern hemisphere seasons to explain the temporal variations of the noise for Winter (Dec-Feb), Spring (Mar-May), Summer (Jun-Aug) and Autumn (Sep-Nov). The results of the four season analysis are available in the Supporting Information (Figs S25–S32).

Visually inspecting the monthly fan diagrams at different passbands investigated in this study, we observe a considerably more
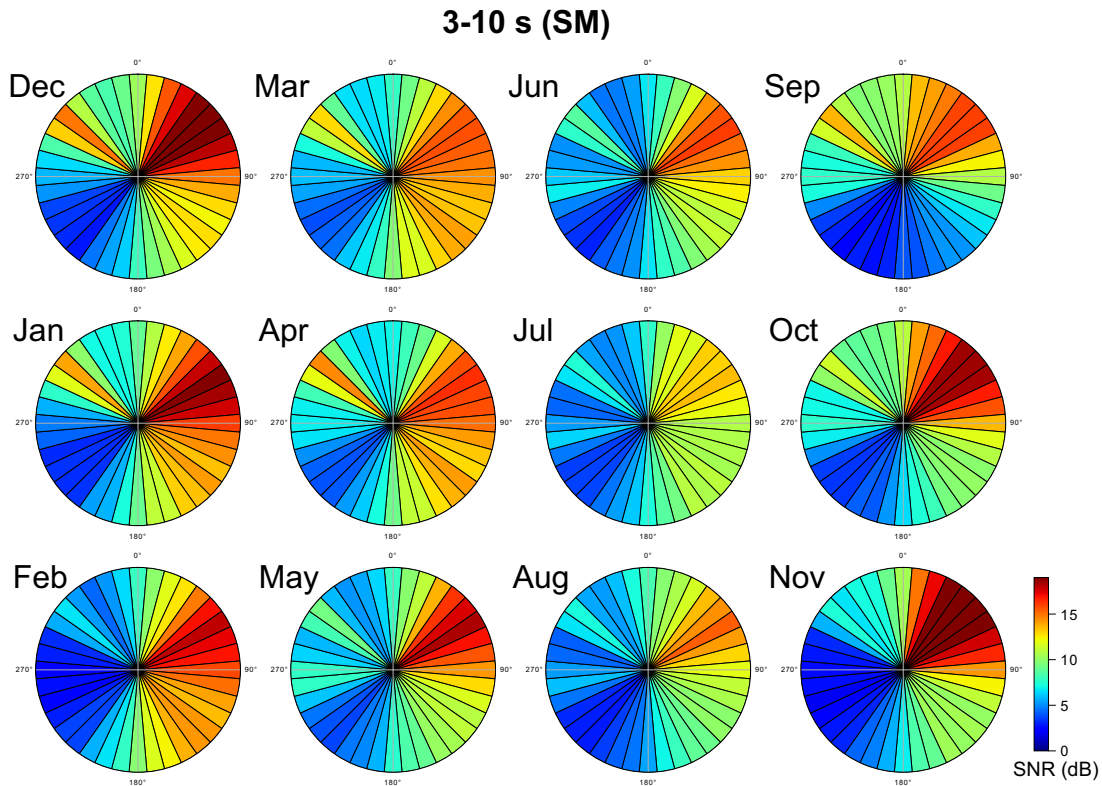
3-10 s (SM)

Figure 8. Monthly variations of the seismic ambient noise for the secondary microseism band (3–10 s). Each fan diagram represents the average results for all stations. Results for subpassbands 3–5 and 5–10 s are also available in the Supporting Information (Figs S21 and S22).
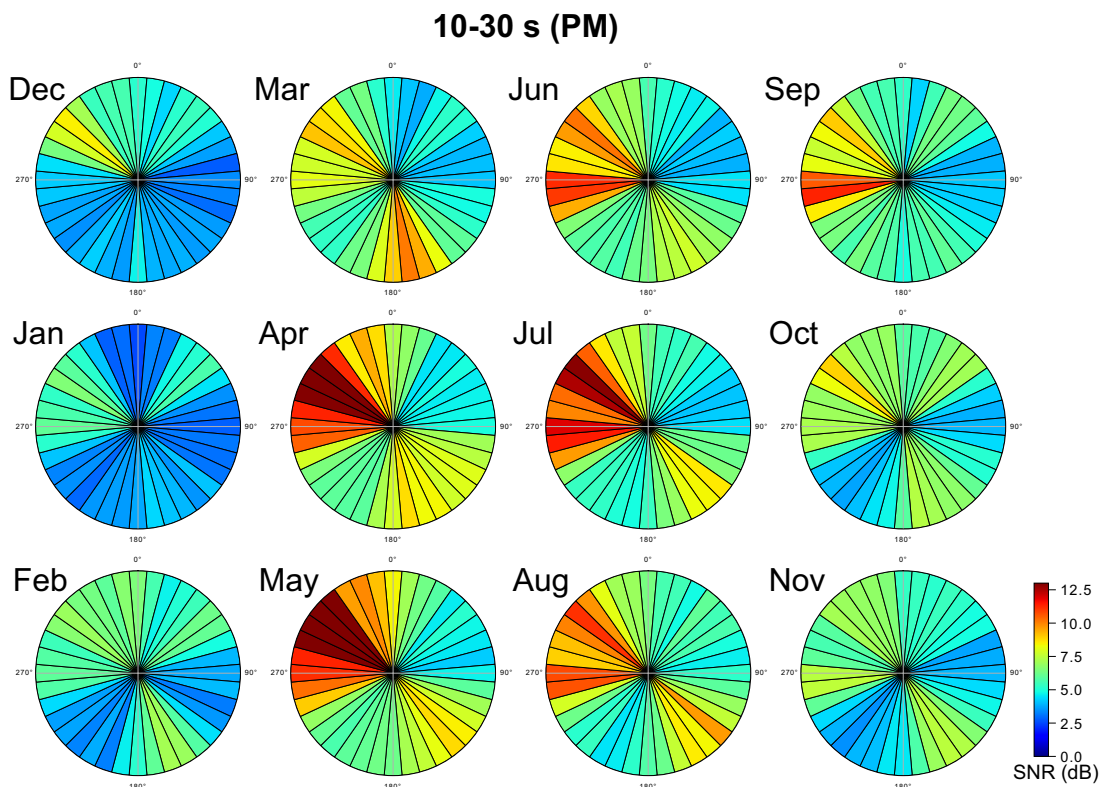
10-30 s (PM)

Figure 9. Monthly variations of the seismic ambient noise for the primary microseism band (10–30 s). Each fan diagram represents the average results for all stations. Results for subpassbands 10–20 and 20–30 s are also available in the Supporting Information (Figs S23 and S24).
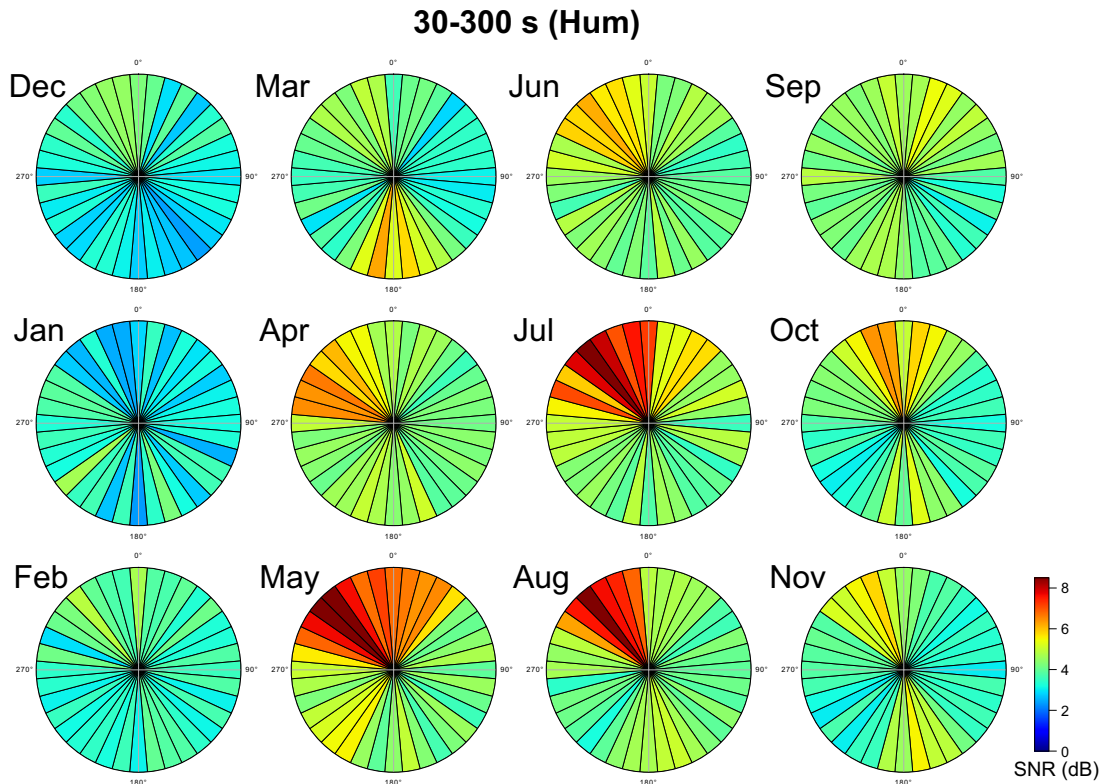
30-300 s (Hum)

Figure 10. Monthly variations of the seismic ambient noise for the seismic hum band (30–300 s). Each fan diagram represents the average results for all stations.

persistent noise distribution at the SM band than the PM and Hum bands. Nonetheless, the observed monthly variation patterns for the SM suggest that this passband is subject to seasonal variations and the arriving signals are generally stronger during the northern hemisphere Winter and Autumn months, especially for the northeast dominant source. The signal arriving from the northwest presents different temporal variations, however. It is generally the weakest in Summer, but in Spring it is as strong as that observed in the Winter months. To gain more understanding of SM temporal variations, we also investigated this passband at two subpassbands of 3–5 s and 5–10 s. The observed patterns of monthly variations in the fan diagrams for 5–10 s are quite similar to those observed at the main SM passband (i.e. 3–10 s). Compared to the short-period SM at 3–5 s, the azimuthal content of the high-SNR arrivals is clearly less variable over time at 5–10 s. That said, the average SNR is relatively more persistent throughout the year at 3–5 s than 5–10 s (Supporting Information Figs S21 and S22). The fact that the SM sources at 5–10 s experience less azimuthal content variations than the sources at 3–5 s was also reported in a recent study across Cape Verde in the North Atlantic Ocean by Carvalho *et al.* (2019). Similar to our study, Carvalho *et al.* (2019) also found that the SM signals during the northern hemisphere Summer are the weakest (Fig. 8).

In contrast to the observations for seasonal variations of the SM, the seismic noise at the PM is strongest during the northern hemisphere Spring and Summer months (Fig. 9; Supporting Information Fig. S29). Unlike the SM band for which the stations receive the strongest noise during Winter, the noise at the PM is the weakest during Winter times. At this passband, the two stronger dominant noise signals arriving from the west and the northwest show slightly different signal level in different months. According to the analysis of the full-stack data sets (directionality analysis), the western

dominant signal is generally weaker than that received from the northwest. The monthly variation fan diagrams, however, suggest that the western signal is sometimes stronger than the signal received from the northwest (in June and September; Fig. 9). Having said that, the difference is small (less than 2 dB) which could be in the range of measurement uncertainties at this passband (Supporting Information Fig. S29). The relatively weaker noise signal propagating from a source in the south to southeast is also stronger in Spring and Summer months, and our seasonality analysis suggests that this source has a relatively more diffuse character than that observed for the stronger signals received from the west and the northwest. The monthly fan diagrams at the main PM band (10–30 s) and subpassband 10–20 s are almost identical. We note that the monthly fan diagrams at subpassbands 20–30 s and the Hum (30–300 s) indicate similar patterns of signal level and azimuthal content variations, but with a ~5 dB stronger signal at the 20–30 s band than the Hum on average.

At the Hum passband (30–300 s), our results suggest that the signals during the Winter are notably weaker than the other seasons, and very close to the background noise level (SNR < 4; Fig. 10; Supporting Information Fig. S32). The strongest Hum signals (SNR > 6 dB) are received from the northwest to the north during the Spring and Summer. The other dominant Hum source located to the south of the study area produces the strongest seismic noise from Spring to Autumn with peak SNR of ~6-7 dB observed in March (Fig. 10; Supporting Information Fig. S32). This source produces a signal with diffuse character and moderate strength with SNR values of about 5–6 dB between April and November (Fig. 10).

Some previous studies have found a correlation between the strength of received Hum signals and hemispheric Winter-time atmospheric events (Rhie & Romanowicz 2004; Nishida & Fukao

2007; Traer *et al.* 2012; Deen *et al.* 2018; Gualtieri *et al.* 2019). Contrary to these studies, our results suggest that the Hum is the weakest during the Winter months (Fig. 10). We suggest that the differences between the observed seasonal variations of the Hum signals in this study and the previous studies could be due to different pre-processing techniques used for removal of unwanted signals, as they did not use the one-bit normalization technique that we used for this purpose. The optimal processing procedure for ambient noise data, especially at long periods, is still a subject of debate (e.g. Bensen *et al.* 2007; Boué *et al.* 2013; Chen *et al.* 2016). A recent study by Wang *et al.* (2021) investigated the effect of using different time-domain clipping threshold methods on their noise directionality analysis results and found no significant changes caused by adopting different techniques. On the other hand, Chen *et al.* (2016) suggested that by using aggressive earthquake removal methods, such as one-bit normalization, sensitivity to detecting short-term noise sources would be significantly reduced. Hence, it is possible that the high-SNR azimuths in our seasonal fan diagrams, especially for the weaker Hum passbands, are overemphasizing the more persistent sources, and understating the effect of sources caused by more transient weather events such as storms. The type of seasonality analysis in this research, based on investigation of the monthly fan diagrams averaged over more than two years of data in 2013–2015, does not allow us to study possible correlation of the SNR variations with short-term severe weather events that may not necessarily reoccur in different years. As a result, this issue merits further research and requires employing a different analysis strategy such as processing and studying daily (rather than two-year monthly averaged) fan diagrams, and comparing the effects of different single-station pre-processing strategies.

6 DISCUSSION

Although it is not possible to infer the exact location of the dominant sources of the ambient seismic noise using a single seismograph array and the back-projection technique, we can still discuss the direction of the stronger arriving noise. We use the results of this study along with previous research to answer fundamental questions about the characteristics of the ambient seismic noise over the two-year period of the data in southeastern Canada and the NE USA.

6.1 Are our results affected by local background noise?

A relatively higher RMS_{noise} would decrease the SNR values, hence a good understanding of variations of this parameter is required for accurate interpretation of the results. We investigated spatial and temporal variations of RMS_{noise} at the different main passbands of the ambient noise, averaged over all azimuthal bins of individual fan diagrams as well as for the entire seismograph network, to see if any systematic variations could be attributed to this parameter (Supporting Information Fig. S33). Interestingly, we find no clear systematic relationship between the variations of the average RMS_{noise} at the stations and their distance from the Atlantic coast. We observe that stations belonging to groups G2 and G3 have much higher RMS_{noise} level than that observed for G1 and G4 at different passbands (Supporting Information Fig. S33). If there was a systematic relation between the RMS_{noise} and the distance from the coast, group G4 would have been among the noisiest along with G3, but this is not suggested by the results. There does not seem to be any systematic in terms of seismograph station sensors and/or installation methods either, as these groups contain a combination of different sensor

types, and both temporary and permanent installations. In terms of its monthly variations, our analysis suggests that RMS_{noise} experiences some small variations over time, but these variations are generally well correlated with the average SNR variations (Supporting Information Fig. S33). This likely suggests that despite our effort to select the EGF noise window such that it does not include coherent signals, the noise window may still contain some coherent content. Nevertheless, these observations suggest that our seasonality analysis results are not affected by the variations of the RMS_{noise} over time. For instance, the Hum and the PM being the weakest during Winter months is not due to a much higher RMS_{noise} during these times (Figs 9–10; Supporting Information Fig. S33).

6.2 Can we use our EGF data sets to obtain unbiased velocity information of the subsurface?

For the two-year noise data used in this study, the signal level inferred from the fan diagrams at all passbands and azimuths is never below the 3 dB threshold, even for the weakest frequency passband of the noise spectrum (i.e. the Hum). In the case of the SM and PM, the minimum SNR for the full-stack fan diagrams is ∼7–8 dB which is a respectable level of signal strength. This indicates that high-quality EGFs are achieved overall for the study area using the two year data set. As mentioned in Section 1, it is still possible to obtain unbiased estimates of phase velocities in the case of a non-uniform noise distribution. Since the final EGF data set provides a dense coverage of crossing interstation paths with a comprehensive azimuthal distribution, and the seismic structure beneath our study area is relatively complex, the inhomogeneous noise field is not expected to cause significant bias in phase-velocity tomography results (Sadeghisorkhani *et al.* 2017; Bagherpur Mojaver & Darbyshire 2022). Based on our analysis, we recommend at least a full year (January to December) of noise data to improve the azimuthal content, the minimum SNR, and also to account for the effect of variable seasonal variations for both the SM and PM bands (Section 5.2).

6.3 Are the PM, SM and the Hum generated at the same locations?

By comparing the directionality and seasonality analysis results at different period passbands, it becomes evident that the SM and PM noise are mostly generated at different locations. There have been other studies that also suggested a different location for generation of ambient seismic noise at the SM and PM bands (e.g. Stehly *et al.* 2006; Tian & Ritzwoller 2015). While the strongest SM signals arrive from the north to southeastern directions (Fig. 7; Supporting Information Fig. S6), the dominant sources generating the strongest noise at the PM band are located in the west to the northwest of our study area (Fig. 7; Supporting Information Fig. S9). As noted in the previous sections, a dominant northwest signal exists in both SM and the PM bands, which is received relatively stronger at the PM band. Although it is observed in both passbands, our analysis suggests significantly different characteristics for this signal for the SM and PM bands. The signal is limited to a relatively narrower azimuthal range at the SM than the PM. It is also the strongest during Winter at the SM as opposed to the results for the PM which indicates that it is the weakest during the Winter months. These observations suggest that this signal is more likely excited at a different location for the SM and PM, despite being received from a similar azimuth.

The long-period PM (20–30 s) arrivals suggest a very similar pattern of seasonal variations to that observed for the Hum (30–300 s). A similar observation was previously noted for the total average fan diagrams (Fig. 7; Supporting Information Figs S11 and S12). To investigate further, we generated extra fan diagrams at 20–50, 50–300 and 50–500 s (Supporting Information Fig. S34). We observe a similar pattern of variations at 20–30 s, 20–50 s and periods longer than 50 s. Putting together these observations, we can infer that the shortest period of the seismic hum may be closer to 20 s than 30 s. The observed differences in azimuthal distribution of the 10–20 s PM subpassband and that of the Hum suggest that their main sources are situated at different locations, even though their temporal variations may suggest a similar generation mechanism (Figs 7, 9 and 10)

6.4 Where are the dominant noise sources located?

Fig. 11 highlights the strongest arriving signals at different passbands investigated in this study. In this figure, great-circle back-projections for the azimuths of the strongest noise signal arrivals at the three main passbands discussed in Section 5.1 are drawn as dotted-dashed lines, and the highlighted areas correspond to the range of azimuths with fan diagram SNR values larger than one standard deviation of the variations at the pertinent passbands. To expand the discussion, we also marked approximate locations of a selection of possible near-coastal and deep-ocean sources for the different passbands of the seismic noise suggested by previous studies (Fig. 11). We note that to infer the exact location of the noise sources excited at different passbands, employing techniques other than our method, such as spherical beam forming (e.g. Zhang *et al.* 2010) or sophisticated noise source inversion techniques (e.g. Ermert *et al.* 2021), along with a spectral analysis (e.g. Ardhuin *et al.* 2015) would be required.

As discussed in Section 5.1, the two SNR peaks in the fan diagrams at the SM band are centred at 60° and 310° azimuths, and the prominent northwestern signal is only observed at 5–10 s. The proposed generation mechanism for the SM can occur in both near-coastal and pelagic areas (Section 1.1). Despite their seasonal signal strength variations, the strongest SM signals at 5–10 s arrive from similar azimuths centered around the northeast and the northwest throughout the year, suggesting that they are likely generated at the same locations (Supporting Information Fig. S22). On the other hand, the dominant SM sources at the shorter periods, 3–5 s, arrive from different azimuths in different months, mainly from directions corresponding to the northeast to southeast in the Atlantic Ocean (Supporting Information Fig. S21). The difference in seasonal variation patterns between the two SM subpassbands may be due to differences in their different excitation locations. In contrast to near coastal-generated SM signals, it is suggested that pelagic SM sources produce signals with a generally longer duration and are therefore less subject to seasonal variations in terms of their dominant azimuthal content (e.g. Chen *et al.* 2016). If correct, this means that our dominant SM sources at 5–10 s may be predominantly situated in pelagic areas, whereas the shorter period SM sources at 3–5 s are more likely excited in near-coastal regions. Some previous studies have also mentioned a similar interpretation for the short and long-period SM generation (e.g. Bromirski *et al.* 2005; Guo *et al.* 2020). Despite the fact that we do not observe any strong signals at 3–5 s arriving from the west, we cannot rule out the possibility of SM sources on the western North American margin. Instead, the lack of a strong western 3–5 s signal could be due to

high attenuation of the SM signals (e.g. Bromirski *et al.* 2005), and this hypothesis merits further research.

Although the primary microseisms arrrive from all directions (SNR > 3), the strongest signals are received from the west to the northwest azimuths suggesting that the principal sources are located in the Pacific Ocean (Fig. 11, Supporting Information Fig. S9). While the majority of previous studies suggest a near-coastal origin for the the PM noise generation mechanism (Section 1.1), the strongest PM noise is observed arriving from the west and not from the nearby Atlantic coasts. In the western USA, Tian & Ritzwoller (2015) also found that the strongest PM signals arrive from an eastern Pacific Ocean area (their fig. 9), which they interpret as offshore sources situated near Vancouver Island and the southern coastline of Oregon. Slightly weaker than these Pacific signals, they also observed dominant PM signals arriving from the north Atlantic azimuths. Interestingly, our analysis suggests that the PM signals arriving from the Pacific Ocean in the west and northwest are significantly stronger than the signals arriving from the eastern azimuths corresponding to the closer Atlantic regions. That said, the corresponding Atlantic PM signals in our study are still prominent, with an average SNR of ∼8–10 dB and a maximum SNR of 15 dB (Section 5.1; Fig. 7; Supporting Information Fig. S29). Although we cannot be certain about the noise source locations, the fact that the PM signals are received with relatively smooth SNR variations over a wide range of azimuths is compatible with the proposed near-coastal generation mechanism suggested for this passband (Section 1.1). One possible reason that we do not see the Atlantic PM signals as strongly as those observed for the Pacific azimuths could be the differences in bathymetry between the eastern and western North American margins, if the hypothesis of near-coastal generation is correct. The reason for the relative weakness of our Atlantic PM signals compared to those suggested by Tian & Ritzwoller (2015) remains an open question, however. It may be that the closest coastal sources only excite a certain frequency range of the PM, with sources at the other side of the North American continent dominating at different PM frequencies (Gualtieri *et al.* 2019), though further study is needed to verify this hypothesis.

The Hum arrivals are the weakest of the ambient seismic noise spectrum, and it is suggested that their generation mechanism, similar to the PM generation, is dominated by direct interaction of the ocean swells with sloping seafloor and seafloor topography (e.g. Ardhuin *et al.* 2015). It is still debated whether the Hum sources are only limited to mainly near-coastal and shallow water-depth regions (e.g. Ardhuin *et al.* 2015), or if they are distributed across the entire oceanic domain (e.g. Nishida & Fukao 2007). Solely relying on the results in this study, which are obtained using a back-projection technique, we cannot infer the exact source location or distance. Nonetheless, we indicate the azimuths corresponding to the directions from which high-SNR signals are received as well as the suggested dominant source regions according to previous studies (Fig. 11).

The strongest Hum signals are received over a wide range of azimuths from the northwest to the north, and also from a relatively weaker and more localized zone in the south (Fig. 11). Although we are not able to locate the exact location of the possible sources and the excitation mechanisms from our results, the proposed generation mechanism for the Hum Rayleigh waves by Ardhuin *et al.* (2015) is compatible with our observations. The high SNR back-projected great-circle paths for the Hum mainly correspond to sources in the northern Pacific Ocean, South American margins, offshore Alaska, as well as the Arctic (Fig. 11), and may originate from ocean wave interactions with continental shelf breaks (e.g. Ardhuin *et al.* 2015).
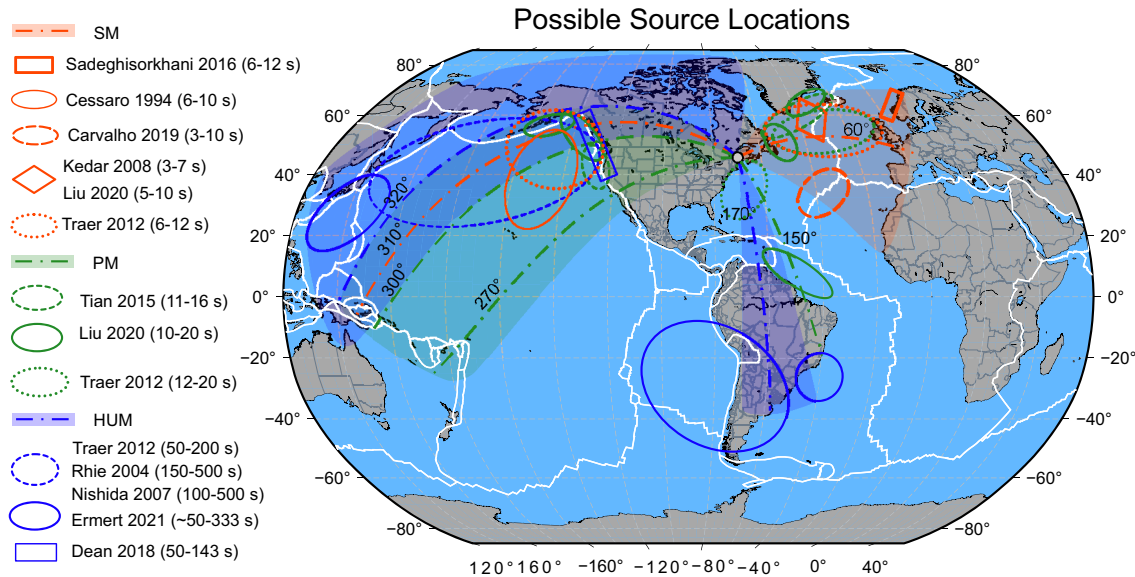
Figure 11. Possible source regions for the SM (orange), PM (green) and the Hum (blue) frequency bands of the ambient seismic noise. The great-circle lines are back-projected for the strongest noise arrivals to the study area (grey circle). The highlighted regions correspond to the azimuthal ranges with signal levels higher than one standard deviation of the measurements in the full-stack fan diagrams at different periods. The regions marked by the different geometrical shapes indicate the approximate locations of the noise generation at different passbands (different colors) suggested by previous studies (Cessaro 1994; Rhie & Romanowicz 2004; Nishida & Fukao 2007; Kedar *et al.* 2008; Traer *et al.* 2012; Tian & Ritzwoller 2015; Sadeghisorkhani *et al.* 2016; Deen *et al.* 2018; Carvalho *et al.* 2019; Liu *et al.* 2020; Ermert *et al.* 2021).

To the best of our knowledge, near-coastal regions in the northern Pacific (Rhie & Romanowicz 2004; Nishida & Fukao 2007; Traer *et al.* 2012; Deen *et al.* 2018), South American margins (Ermert *et al.* 2021), and offshore Alaska (Rhie & Romanowicz 2004; Nishida & Fukao 2007; Traer *et al.* 2012) have been previously suggested as domains of strong Hum generation sources, but strong Hum arrivals from the Arctic are suggested for the first time in this study. We also note that the Hum arriving from the south corresponds to an oceanic region where the occurrence of Atlantic storms and hurricanes is very frequent during the Summer and Autumn seasons. Although our monthly fan diagrams that are averaged over two years may not be sensitive to detecting individual North Atlantic storms or hurricanes, stronger Hum signals received from the corresponding azimuths in Summer and Autumn seasons may reflect an overall increase of noise caused by the prevalence of storms during these seasons (Fig. 10; Supporting Information Fig. S32), and this issue merits further research. Infragravity ocean waves caused by storms and hurricanes can generate seismic noise at the Hum passband (e.g. Ardhuin *et al.* 2015).

7 CONCLUSIONS

Using a back-projection technique applied to EGFs generated from more than two years of noise data, we studied directional and seasonal variations of ambient seismic noise in southeastern Canada and the NE USA. We modified the existing definition of fan diagram representation to include both causal and acausal signals in the statistical analysis of the noise strength and azimuthal content. This new definition enables us to analyse the noise distribution with higher accuracy as more data is used in the generation of resulting fan diagrams. Our analysis suggests that spatial and temporal variations of the local background noise do not necessarily correlate with station distance from the coast, and our results are not affected by the variations of the local background noise. Despite being located

in an area that is subject to strong inhomogeneous noise distribution effects, high-quality EGFs with sufficiently large SNR signals arrive from all directions to the study area which makes it possible to use the same EGF data sets to obtain unbiased tomographic models. The main passbands of the seismic noise spectrum, namely the SM (3–10 s), the PM (10–30 s) and the Hum (30–300 s) along with a few subpassbands for the SM and PM were investigated. We conclude that the dominant sources for generation of these three passbands (SM, PM and Hum) are situated at different locations in the Pacific, Atlantic and Arctic oceans.

DATA AVAILABILITY

The seismic data used in this study are archived at the IRIS Data Management Center [http://www.iris.edu/hq/; http://ds.iris.edu/ds/nodes/dmc/; networks (CN; Geological Survey of Canada 1989), (NE; ASL/USGS 1994), (TA; IRIS Transportable Array 2003), (PO; Eaton *et al.* 2005), (X8, Y8; Menke *et al.* 2012; SEIS-UK 2013)] or at the Canadian National Data Center, Natural Resources Canada [https://earthquakescanada.nrcan.gc.ca/stndon/index-en.php; (CN; Geological Survey of Canada 1989)].

REFERENCES

Ardhuin, F., Stutzmann, E., Schimmel, M. & Mangeney, A., 2011. Ocean wave sources of seismic noise, *J. geophys. Res.,* **116** . doi:10.1029/2011JC006952.

Ardhuin, F., Gualtieri, L. & Stutzmann, E., 2015. How ocean waves rock the Earth: Two mechanisms explain microseisms with periods 3 to 300 s, *Geophys. Res. Lett.,* **42,** 765–772.

ASL/USGS, 1994. *New England Seismic Network,* International Federation of Digital Seismograph Networks.

Bagherpur Mojaver, O. & Darbyshire, F., 2022. Crustal structure beneath the northern Appalachians and the eastern Grenville Province, *J. geophys. Res.,* **127,** e2021JB023246. doi:10.1029/2021JB023246.

Behr, Y., Townend, J., Bowen, M., Carter, L., Gorman, R., Brooks, L. & Bannister, S., 2013. Source directionality of ambient seismic noise inferred from three-component beamforming, *J. geophys. Res.,* **118,** 240–248.

Bensen, G., Ritzwoller, M., Barmin, M., Levshin, A.L., Lin, F., Moschetti, M., Shapiro, N. & Yang, Y., 2007. Processing seismic ambient noise data to obtain reliable broad-band surface wave dispersion measurements, *Geophys. J. Int.,* **169,** 1239–1260.

Boué, P., Poli, P., Campillo, M., Pedersen, H., Briand, X. & Roux, P., 2013. Teleseismic correlations of ambient seismic noise for deep global imaging of the Earth, *Geophys. J. Int.,* **194,** 844–848.

Bromirski, P.D., Duennebier, F.K. & Stephen, R.A., 2005. Mid-ocean microseisms, *Geochem. Geophys. Geosyst.,* **6,** doi:10.1029/2004GC000768.

Carvalho, J.F., Silveira, G., Schimmel, M. & Stutzmann, E., 2019. Characterization of microseismic noise in Cape Verde, *Bull. seism. Soc. Am.,* **109,** 1099–1109.

Cessaro, R.K., 1994. Sources of primary and secondary microseisms, *Bull. seism. Soc. Am.,* **84,** 142–148.

Chen, Z., Gerstoft, P. & Bromirski, P.D., 2016. Microseism source direction from noise cross-correlation, *Geophys. J. Int.,* **205,** 810–818.

Cupillard, P. & Capdeville, Y., 2010. On the amplitude of surface waves obtained by noise correlation and the capability to recover the attenuation: a numerical approach, *Geophys. J. Int.,* **181,** 1687–1700.

Deen, M., Stutzmann, E. & Ardhuin, F., 2018. The earth's hum variations from a global model and seismic recordings around the Indian ocean, *Geochem. Geophys. Geosyst.,* **19,** 4006–4020.

Eaton, D. & et, al., 2005. Investigating Canada's lithosphere and earthquake hazards with portable arrays, *EOS, Trans. Am. geophys. Un.,* **86,** 173.

Ermert, L.A., Sager, K., Nissen-Meyer, T. & Fichtner, A., 2021. Multifrequency inversion of global ambient seismic sources, *Geophys. J. Int.,* **225,** 1616–1623.

Fichtner, A., 2014. Source and processing effects on noise correlations, *Geophys. J. Int.,* **197,** 1527–1531.

Geological Survey of Canada, 1989. *Canadian National Seismograph Network,* International Federation of Digital Seismograph Networks.

Gerstoft, P. & Tanimoto, T., 2007. A year of microseisms in southern California, *Geophys. Res. Lett.,* **34,** doi:10.1029/2007GL031091.

Gualtieri, L., Stutzmann, E., Juretzek, C., Hadziioannou, C. & Ardhuin, F., 2019. Global scale analysis and modelling of primary microseisms, *Geophys. J. Int.,* **218,** 560–572.

Guo, Z., Xue, M., Aydin, A. & Ma, Z., 2020. Exploring source regions of single-and double-frequency microseisms recorded in eastern North American margin (ENAM) by cross-correlation, *Geophys. J. Int.,* **220,** 1352–1367.

Gutenberg, B., 1936. On microseisms, *Bull. seism. Soc. Am.,* **26,** 111–117.

Haned, A., Stutzmann, E., Schimmel, M., Kiselev, S., Davaille, A. & Yelles-Chaouche, A., 2016. Global tomography using seismic hum, *Geophys. J. Int.,* **204,** 1222–1236.

Harmon, N., Rychert, C. & Gerstoft, P., 2010. Distribution of noise sources for noise derived Green's functions, *Geophys. J. Int.,* **183,** 1470–1484.

Hasselmann, K., 1963. A statistical analysis of the generation of microseisms, *Rev. Geophys.,* **1,** 177–210.

Hunter, J.D., 2007. Matplotlib: a 2D graphics environment, *Comput. Sci. Eng.,* **9,** 90–95.

IRIS Transportable Array, 2003. *USArray Transportable Array,* International Federation of Digital Seismograph Networks.

Kao, H. *et al.* 2013. Ambient seismic noise tomography of Canada and adjacent regions: Part I. Crustal structures, *J. geophys. Res.,* **118,** 5865–5887.

Kedar, S., Longuet-Higgins, M., Webb, F., Graham, N., Clayton, R. & Jones, C., 2008. The origin of deep ocean microseisms in the North Atlantic Ocean, *Proc. R. Soc. A,* **464,** 777–793.

Köhler, A., Weidle, C. & Maupin, V., 2011. Directionality analysis and Rayleigh wave tomography of ambient seismic noise in southern Norway, *Geophys. J. Int.,* **184,** 287–300.

Kuponiyi, A.P., Kao, H., van Staal, C.R., Dosso, S.E., Cassidy, J.F. & Spence, G.D., 2017. Upper crustal investigation of the Gulf of Saint Lawrence region, eastern Canada using ambient noise tomography, *J. geophys. Res.,* **122,** 5208–5227.

Liu, C., Aslam, K. & Langston, C.A., 2020. Directionality of ambient noise in the Mississippi embayment, *Geophys. J. Int.,* **223,** 1100–1117.

Longuet-Higgins, M.S., 1950. A theory of the origin of microseisms, *Phil. Trans. R. Soc. Lond., A,* **243,** 1–35.

Macquet, M., Paul, A., Pedersen, H.A., Villaseñor, A., Chevrot, S., Sylvander, M., Wolyniec, D. & Group, P.W., 2014. Ambient noise tomography of the Pyrenees and the surrounding regions: inversion for a 3-D Vs model in the presence of a very heterogeneous crust, *Geophys. J. Int.,* **199,** 402–415.

Menke, W., Levin, V. & Darbyshire, F.A., 2012. *Deep Structure of Three Continental Sutures in Eastern North America (QM-III),* International Federation of Digital Seismograph Networks.

Nakata, N., Gualtieri, L. & Fichtner, A., 2019. *Seismic Ambient Noise,* Cambridge Univ. Press.

Nishida, K. & Fukao, Y., 2007. Source distribution of Earth's background free oscillations, *J. geophys. Res.,* **112,** doi:2006JB004720.

Poan, E., Gachon, P., Laprise, R., Aider, R. & Dueymes, G., 2018. Investigating added value of regional climate modeling in North American winter storm track simulations, *Clim. Dyn.,* **50,** 1799–1818.

Poli, P., Thomas, C., Campillo, M. & Pedersen, H.A., 2015. Imaging the D" reflector with noise correlations, *Geophys. Res. Lett.,* **42,** 60–65.

Retailleau, L., Boué, P., Li, L. & Campillo, M., 2020. Ambient seismic noise imaging of the lowermost mantle beneath the north Atlantic Ocean, *Geophys. J. Int.,* **222,** 1339–1351.

Rhie, J. & Romanowicz, B., 2004. Excitation of Earth's continuous free oscillations by atmosphere–ocean–seafloor coupling, *Nature,* **431,** 552–556.

Sabra, K.G., Gerstoft, P., Roux, P., Kuperman, W.A. & Fehler, M.C., 2005. Extracting time-domain Green's function estimates from ambient seismic noise, *Geophys. Res. Lett.,* **32,** doi:10.1029/2004GL021862.

Sadeghisorkhani, H., Gudmundsson, Ó., Roberts, R. & Tryggvason, A., 2016. Mapping the source distribution of microseisms using noise covariogram envelopes, *Geophys. J. Int.,* **205,** 1473–1491.

Sadeghisorkhani, H., Gudmundsson, Ó., Roberts, R. & Tryggvason, A., 2017. Velocity-measurement bias of the ambient noise method due to source directivity: a case study for the Swedish National Seismic Network, *Geophys. J. Int.,* **209,** 1648–1659.

SEIS-UK, 2013. *QM-III Network—Atlantic Canada,* International Federation of Digital Seismograph Networks.

Shapiro, N.M. & Campillo, M., 2004. Emergence of broadband Rayleigh waves from correlations of the ambient seismic noise, *Geophys. Res. Lett.,* **31,** doi:10.1029/2004GL019491.

Shapiro, N.M., Campillo, M., Stehly, L. & Ritzwoller, M.H., 2005. High-resolution surface-wave tomography from ambient seismic noise, *Science,* **307,** 1615–1618.

Shapiro, N.M., Ritzwoller, M. & Bensen, G., 2006. Source location of the 26 sec microseism from cross-correlations of ambient seismic noise, *Geophys. Res. Lett.,* **33,** doi:10.1029/2006GL027010.

Sleep, N.H., 1990. Monteregian hotspot track: a long-lived mantle plume, *J. geophys. Res.,* **95,** 21 983–21 990.

Stehly, L. & Boué, P., 2017. On the interpretation of the amplitude decay of noise correlations computed along a line of receivers, *Geophys. J. Int.,* **209,** 358–372.

Stehly, L., Campillo, M. & Shapiro, N., 2006. A study of the seismic noise from its long-range correlation properties, *J. geophys. Res.,* **111,** doi:10.1029/2005JB004237.

Tian, Y. & Ritzwoller, M.H., 2015. Directionality of ambient noise on the Juan de Fuca plate: implications for source locations of the primary and secondary microseisms, *Geophys. J. Int.,* **201,** 429–443.

Tkalčić, H., Pham, T.S. & Wang, S., 2020. The Earth's coda correlation wavefield: Rise of the new paradigm and recent advances, *Earth-Sci. Rev.,* **208,** 103285, doi:10.1016/j.earscirev.2020.103285.

Traer, J., Gerstoft, P., Bromirski, P.D. & Shearer, P.M., 2012. Microseisms and hum from ocean surface gravity waves, *J. geophys. Res.,* **117,** doi:10.1029/2012JB009550.

Tsai, V.C., 2011. Understanding the amplitudes of noise correlation measurements, *J. geophys. Res.,* **116,** doi:10.1029/2011JB008483.

van Staal, C.R. & Barr, S., 2012. Lithospheric architecture and tectonic evolution of the Canadian Appalachians and associated Atlantic margin, *Tectonic styles in Canada: The LITHOPROBE perspective: Geological Association of Canada Special Paper,* **49,** 41–95.

Wang, S. & Tkalčić, H., 2020a. Seismic event coda-correlation: toward global coda-correlation tomography, *J. geophys. Res.,* **125,** e2019JB018848, doi:10.1029/2019JB018848.

Wang, S. & Tkalčić, H., 2020b. Seismic event coda-correlation's formation: implications for global seismology, *Geophys. J. Int.,* **222,** 1283–1294.

Wang, Z., Niu, F., Huang, J., Li, Z. & Chen, H., 2021. Distribution of Rayleigh wave microseisms constrained by multiple seismic arrays, *J. geophys. Res.,* **126,** e2021JB022084, doi:10.1029/2021JB022084.

Wessel, P., Smith, W.H., Scharroo, R., Luis, J. & Wobbe, F., 2013. Generic mapping tools: improved version released, *EOS, Trans. Am. geophys. Un.,* **94,** 409–410.

Yang, Y. & Ritzwoller, M.H., 2008. Characteristics of ambient seismic noise as a source for surface wave tomography, *Geochem. Geophys. Geosyst.,* **9,** doi:10.1029/2007GC001814.

Yang, Y., Li, A. & Ritzwoller, M.H., 2008. Crustal and uppermost mantle structure in southern Africa revealed from ambient noise and teleseismic tomography, *Geophys. J. Int.,* **174,** 235–248.

Yao, H., van Der Hilst, R.D. & De Hoop, M.V., 2006. Surface-wave array tomography in SE Tibet from ambient seismic noise and two-station analysis—I. Phase velocity maps, *Geophys. J. Int.,* **166,** 732–744.

Zeng, X. & Ni, S., 2010. A persistent localized microseismic source near the Kyushu Island, Japan, *Geophys. Res. Lett.,* **37,** doi:10.1029/2010GL045774.

Zhang, J., Gerstoft, P. & Bromirski, P.D., 2010. Pelagic and coastal sources of *P*-wave microseisms: generation under tropical cyclones, *Geophys. Res. Lett.,* **37,** doi:10.1029/2010GL044288.

SUPPORTING INFORMATION

Supplementary data are available at *GJI* online

S1. Datasets and empirical Green's functions (EGFs)
S2. Fan diagrams - directionality analysis
S3. Fan diagrams - seasonality analysis
S4. Spatial and temporal variations of local background noise
S5. Figures S1 to S34
S6. Table S1

Please note: Oxford University Press is not responsible for the content or functionality of any supporting materials supplied by the authors. Any queries (other than missing material) should be directed to the corresponding author for the paper.